Effects of Non-Photosynthetic Vegetation on Dust Emissions

Xinyue Huang[1] and Hosein Foroutan[1]

[1]Department of Civil and Environmental Engineering, Virginia Tech, Blacksburg, Virginia, USA

Corresponding author: Hosein Foroutan (hosein@vt.edu)

Key Points:

- A satellite-based total vegetation dataset is implemented in a dust emission model
- Non-photosynthetic vegetation (NPV) reduces dust concentrations by over 10% in most areas of the southwestern U.S. from spring to autumn
- NPV suppresses dust emissions mainly by sheltering the ground surface and raising the threshold velocity

Abstract

Mineral dust is among the top contributors to global aerosol loads and is an active element in the Earth system. Ability of non-photosynthetic vegetation (NPV) to suppress dust emission has been supported by observations and small-scale studies, but current regional to global scale models fail to include NPV in the vegetation coverage input. In this study, we implemented a satellite-based total vegetation data, which included NPV, into a regional atmospheric chemistry model and conducted simulations of the entire year 2016 for the conterminous United States. We also conducted a control simulation using only the photosynthetic vegetation (PV) to analyze the effects of NPV on dust emissions. Above 10% decreases in simulated dust emissions are seen over most of the southwestern United States from spring to autumn due to NPV. Reductions in dust concentrations are the largest in spring, and when compared to observations, attenuate the overpredictions of fine soil concentrations at over 93% of the observation sites in the western U.S. Further analyses of essential parameters to the inclusion of NPV indicate that sheltering the surface and increasing the threshold velocity through drag partitioning are major mechanisms for the suppression of dust emissions. On the other hand, NPV causes the friction velocity to increase by more than 10% over most erodible lands during autumn and winter, which can amplify the dust flux. This study highlights the necessity of including NPV into the dust model and states that uncertainty analyses of total vegetation datasets are important.

Plain Language Summary

Severe dust-emission events can interrupt traffic, damage infrastructure, and incur cleaning expenses locally. Dust particles that are lifted into the air by wind are also associated with global health problems and climate effects. Most of the global dust emissions come from arid or semi-arid environments where the brown vegetation is abundant, and the amount of dust emissions is thus modulated by the presence of brown vegetation. However, current atmospheric models omit brown vegetation because it cannot be detected easily similar to green vegetation. In this study, we provided a total vegetation (sum of green and brown vegetation) dataset as an input to an atmospheric chemistry model, and simulated annual dust emissions over the conterminous United States. We find that the brown vegetation reduces the dust concentrations in air by above 10% over most of the southwestern U.S. from spring to autumn. The reductions are mainly because the brown vegetation directly protects the surface from wind erosion, as well as reduces the drag on the surface such that a minimum wind speed needed to initiate dust emissions becomes higher.

1. Introduction

Mineral dust aerosols emitted by wind erosion play an active role in affecting human health and activities (Baddock et al., 2014; Nakao et al., 2018; Al-Hemoud et al., 2019), impacting the climate (Miller, 1998; Schepanski, 2018), and transporting nutrients and microorganisms (Csavina et al., 2012; Kellogg & Griffin, 2006). The global emissions of dust particles are mainly from arid or semi-arid environments (Knippertz, 2017) and are modulated by non-photosynthetic vegetation (NPV), which is predominant in these regions (Jacques et al.,2014). NPV includes dead leaves, crop residuals, and litters (Guerschman et al., 2009; Ji et al., 2020). Negative relations between the amount of dead leaves on the ground and the frequency of dust outbreaks are supported by interannual observations (Kurosaki et al., 2011; Nandintsetseg & Shinoda, 2015). Also, the relations between soil erosion and the coverage of

flat and standing crop residues were quantified, and the underlying mechanisms were studied on small scale uniform or experimental fields (Hagen, 1996; Lin et al., 2021).

The challenge to extend this knowledge to regional-to-global scales lays in providing accurate information about the temporally and spatially variant vegetation to atmospheric models. In practice, the parameterization of vegetation in windblown dust schemes implemented in current chemical transport models or general circulation models relies on data for vegetation fractional coverage (Duncan Fairlie et al., 2007; Foroutan et al., 2017; LeGrand et al., 2019; Zhang et al., 2012). However, the vegetation fractional maps used by these models are often based on readily available vegetation indices from satellite retrievals which only represents photosynthetic vegetation (PV) (e.g., fraction of absorbed photosynthetically active radiation (FPAR) or normalized difference vegetation index (NDVI)).

To the authors' knowledge, there has been only one attempt to address this failure of accounting for NPV in the vegetation map used to simulate regional dust emissions (Kang et al., 2014). The researchers estimated the NPV fractions in East Asia by assuming that the NPV fractions follow a linear decrease from the maximum fractions of green vegetation from last year. The conclusion that the approximated NPV fractions improved the simulation for a dust event can be further validated with a more realistic representation of NPV coverage that accounts for the non-linear growth-decay cycle of plants in different environments. The total vegetation (sum of PV and NPV) data was made available in the Multiscale Online Non-Hydrostatic AtmospheRe CHemistry (MONARCH) model version 2.0 model as recently reported (Klose et al., 2021) and more studies on the relations between NPV and dynamics of dust emissions are anticipated.

Remote sensing techniques have a high potential to capture the heterogeneity of vegetation compared to field measurements or ecosystem modeling at a larger scale (Mougin et al., 1995). These techniques can identify NPV elements based on their different reflectance spectrum in the visible light to short-wave inferred regions, due to their lower pigments and water contents than PV, and higher cellulose and lignin contents than soils (Z. Li & Guo, 2015). Multispectral imagery is more widely used than hyperspectral imagery at large scales due to availability (Z. Li & Guo, 2015). Several vegetation indices that represent NPV coverage calculated from selected bands of multispectral reflectance have been developed, such as the Normalized Difference Senescent Vegetation Index (NDSVI) (Qi & Wallace, 2002), the Soil Adjusted Total Vegetation Index (SATVI) (Marsett et al., 2006), and the Dead Fuel Index (DFI) (Cao et al., 2010), but they are generally considered to be site-specific (X. Li et al., 2016). Another technique to acquire NPV fractions is the spectral mixture analysis (SMA) which uses all bands of the reflectance spectrum (Asner & Heidebrecht, 2002). The SMA method assumes that the surface reflectance is a combination of the reference reflectance of certain surface components or endmembers, and then resolves the fractions of all endmembers given their reference spectra. Variations of SMA methods (X. Li et al., 2016; Okin et al., 2013) mostly differ in the selection of reference spectra and comparisons among these variations showed that allowing the spectra for a certain endmember to vary among pixels improved the estimation of fractions.

This study is aimed at testing the effects of NPV on the seasonal dust emissions, and understanding the underlying mechanisms. We implemented satellite-based maps for both PV and NPV fractions derived using a SMA method into the windblown dust scheme in the Community Multiscale Air Quality (CMAQ) model and conducted simulations for the entire

year 2016 over the conterminous United States (CONUS) (hereafter the TOTAL run). We also conducted a control run with PV only coverage data represented by the FPAR from the Moderate Resolution Imaging Spectroradiometer (MODIS) instrument (hereafter the FPAR run) and then contrasted the results. Section 2 describes the methods for generating the vegetation data, the parameterization of vegetation in our dust model, and the evaluation methodology. The results are presented and discussed in Section 3. Finally, summaries of our major findings, discussion of uncertainties, and future improvements are included in Section 4.

2. Methods

2.1. Vegetation Data

In this study, we used two datasets for vegetation fractional coverage. The total vegetation data was obtained from the MODIS Nadir BRDF-Adjusted Reflectance (MCD43A4) product collection 5, which has a spatial and temporal resolution of 500 m and every 16 days, respectively. Details about the spectral unmixing analysis (SMA) method used to develop this dataset have been described in Guerschman et al. (2015) and Scarth et al. (2011). In brief, a linear unmixing method was performed to calculate the fractions of three pure surface components, namely PV, NPV, and bare soils based on the observed surface reflectance and the synthetic reference reflectance of the three components. Synthetic reference reflectance was derived from field measurements of vegetation fractional cover and satellite imagery using a multiple regression model. Seven bands of the reflectance from the MCD43A4 product were used to perform the unmixing, as well as their log transforms and interactive terms to account for the non-linear spectral mixing. To avoid overfitting, a subspace truncation method was applied to control the number of reflectance terms used for unmixing and that number was determined with a 100-fold cross-validation method. During the unmixing, the three fractions in each pixel were constrained to be non-negative and must add up to 100%. The resulting dataset includes monthly averaged vegetation fractions at 5 km resolution. It was re-gridded to 12 km over the study domain using the nearest-neighbor space-filling method. The processed monthly data was then transformed into daily data using linear interpolation, and meanwhile, some missing values were replaced using values from consecutive months. For a small amount of grid cells with missing values throughout the year, the total vegetation fractions were set to be 1. The rationale was that the missing values were likely due to snow cover because most of those grids were in the north of the study domain, and a complete coverage of vegetation would eliminate the dust emissions from these cells just as snow cover. Details about this dataset are discussed in Section 3.1.

The other dataset uses an index for green vegetation, the fraction of photosynthetic active radiation (FPAR). The FPAR data was retrieved from the MODIS15A2GFS satellite product with 1 km resolution and every 8 days and then re-gridded and interpolated to a daily 12 km-resolution dataset. This approach and the resulting dataset have been previously used in WRF-CMAQ simulations by Ran et al. (2016) and Foroutan and Pleim (2017).

2.2. Parameterization of Vegetation in the Dust Model

The windblown dust scheme used in CMAQ is a physics-based model described in details by Foroutan et al. (2017). Here, we present a short overview of the scheme and focus on the representation of vegetation in the model. Saltation bombardment is deemed as the main

mechanism of aeolian dust emissions. The module calculates the bulk dust emission and assigns the total mass into fine and coarse modes. The total mass of vertical dust flux is determined based on a horizontal flux and a vertical-to-horizontal flux ratio. The latter is dependent on soil properties and scales with the friction velocity (Lu & Shao, 1999). The total horizontal dust flux is calculated by integrating the horizontal fluxes of particles in each size bin:

$$F_H(D) = \begin{cases} C\frac{\rho_a}{g}u_*^3\left(1-\frac{u_{*,t}(D)}{u_*}\right)\left(1+\frac{u_{*,t}(D)}{u_*}\right)^2, u_{*,t} < u_* \\ 0, \quad u_{*,t} \geq u_* \end{cases} \quad (1)$$

where C is a constant of proportionality set to 1.0, ρ_a is the air density, and $u_{*,t}$ is the threshold friction velocity.

The threshold friction velocity governs the initiation of saltation. It is modeled as an ideal threshold friction velocity corrected with two factors for soil moisture and roughness elements.

$$u_{*,t} = u_{*,t0} f_m f_r \quad (2)$$

Here, $u_{*,t0}$ is the ideal threshold velocity for dry and smooth surfaces. The f_m and f_r are correction factors for soil moisture and surface roughness, respectively, both of which are equal or greater than 1.0. The soil moisture factor is determined according to a model by F. FeÂcan (1999). The roughness factor is determined using a double drag partitioning concept to take both the solid elements and the vegetation into account (Darmenova et al., 2009; Raupach et al., 1993).

$$f_r = (1-\sigma_V m_V \lambda_V)^{0.5}(1+\beta_V m_V \lambda_V)^{0.5}\left(1-\sigma_S m_S \frac{\lambda_S}{1-A_V}\right)^{0.5}\left(1+\beta_S m_S \frac{\lambda_S}{1-A_V}\right)^{0.5} \quad (3)$$

Here, σ_V and σ_S are the basal-to-frontal area ratios of vegetation and solid elements, β_V and β_S are ratios of drag coefficients on vegetation and solid elements to the drag coefficient on bare surface, m_V and m_S account for the differences between average surface stress and maximum surface stress, A_V is the fractional coverage of total vegetation, and λ_V and λ_S are surface roughness density of vegetation and solid elements. We used the same values as Darmenova et

al. (2009) for σ_V, σ_S, β_V, β_S, m_V, and m_S. Values for λ_S for each landuse type were adapted from Xi and Sokolik (2015) and Darmenova et al. (2009).

The λ_V is calculated from vegetation coverage, A_V following a relation proposed by Shao et al. (1996).

$$\lambda_V = -0.35 \ln(1 - A_V) \tag{4}$$

According to Foroutan et al. (2017), the surface wind friction velocity should be corrected for dust emissions calculations:

$$u_* = \kappa U_{10} \ln\left(\frac{z_0}{10}\right) \tag{5}$$

where κ is the von Kármán constant, U_{10} is the 10-m wind speed, and z_0 is the surface roughness length relevant to dust emission processes.

The z_0 scales with the physical height of roughness elements on the surface. To determine z_0, we adapted the empirical relation developed by Foroutan et al. (2017).

$$z_0/h = \begin{cases} 0.96\lambda^{1.07}, \lambda < 0.2 \\ 0.083\lambda^{-0.46}, \lambda \geq 0.2 \end{cases} \tag{6}$$

where λ is the total roughness density, and it is defined as the sum of roughness density for solid elements and total vegetation ($\lambda=\lambda_S+\lambda_V$). The h is the total effective height of roughness elements. In this study, the effective heights of roughness components were updated with the inclusion of NPV. It was calculated as the weighted average of roughness heights based on roughness density:

$$h = \frac{h_{PV}\lambda_{PV} + h_{NPV}\lambda_{NPV} + h_s\lambda_s}{\lambda_{PV} + \lambda_{NPV} + \lambda_s} \tag{7}$$

The set of vegetation heights in Foroutan et al. (2017) basically represents the growth-decay cycle of green vegetation and they were preserved to serve as the height for PV (h_{PV}) in this study (Table 1). Since the phenological and geometric characteristics of dead plant and litter are different from that of PV, a look-up table for the NPV heights were predefined and added to the model. The assignment of the NPV heights considered the seasonal variation, which was implied from the trends of biomass observed in field measurements and modeling practices (Nandintsetseg & Shinoda, 2015; Pierre et al., 2015). The NPV heights reaches their peak in September or October, which is consistent with the evidence that the biomass of senescent plants in grassland peaked between September and November and that the interannual averaged senescence period for typical steppe plants was between September and October (Shinoda et al., 2011). Considering the biomass of NPV did not exceed the biomass of PV, the maximum heights

for NPV were set to be lower than the maximum PV heights. These features were captured in the assigned heights for NPV as shown in Table 1.

Table 1. Predefined Heights for PV and NPV. All units are in cm.

		Jan	Feb	Mar	Apr	May	Jun	Jul	Aug	Sep	Oct	Nov	Dec
Shrubland	PV	5	5	15	15	12	12	10	10	10	5	5	5
	NPV	6	6	5	5	5	5	5	5	6	8	8	6
Grass	PV	5	5	5	10	20	15	12	12	10	5	5	5
	NPV	8	5	5	5	5	5	5	5	10	10	8	8
Barren	PV	5	5	10	10	10	10	10	10	10	10	5	5
	NPV	4	4	4	3	3	3	3	3	5	5	5	5
Crop	PV	5	5	5	5	10	30	50	50	30	10	5	5
	NPV	8	8	5	5	5	5	5	5	15	15	10	10

In general, it can be seen that the vegetation coverage is as an important component of the dust scheme which not only determines the fractions of available surface to wind erosion, but also alters the friction velocity u_* (via surface roughness length, Eq. (6)) and its threshold value $u_{*,t}$ (via surface roughness factor, Eq. (3)).

2.3. Model Setup

The CMAQ model version 5.3 (Appel et al., 2020) was used in this study. The model domain consisting of the CONUS, as well as parts of Mexico and Canada (Figure 1) was discretized using a 12-km horizontal grid and 35 vertical layers. Simulations were performed for the entire year 2016 with a clean initial condition and 10-day spin-up time. The meteorological inputs to CMAQ were generated by a Weather Research and Forecasting (WRF) model version 3.8 simulation and then processed with the Meteorology-Chemistry Interface Processor (MCIP) version 5.0. Anthropogenic emissions input data was provided by the emissions modeling platform run by US EPA and biogenic emissions were calculated in-line. The boundary conditions were derived from hemispheric simulations of CMAQv53. The Biogenic Emission Landcover Database version 3 (BELD3) was used in the dust scheme and three land use types were considered as erodible land, namely USGS_shrubland, USGS_shrubgrass, and USGS_sprsbarren. The total fractions of these three types of erodible lands are shown in Figure 1. The soil type information was based on US State Soil Geographic (STATSGO) soil database (R. L. Miller, 1998) and four soil textures (clay, silt, fine-to-medium sand, and coarse sand) were identified for each soil type following Tegen et al. (2002). Ammonia bi-directional flux and updated M3dry model were used for deposition. CB06r3 chemical mechanism and AERO7

aerosol model were used for atmospheric chemistry. Details on all other settings as well as the model evaluation can be found in Appel et al. (2020).

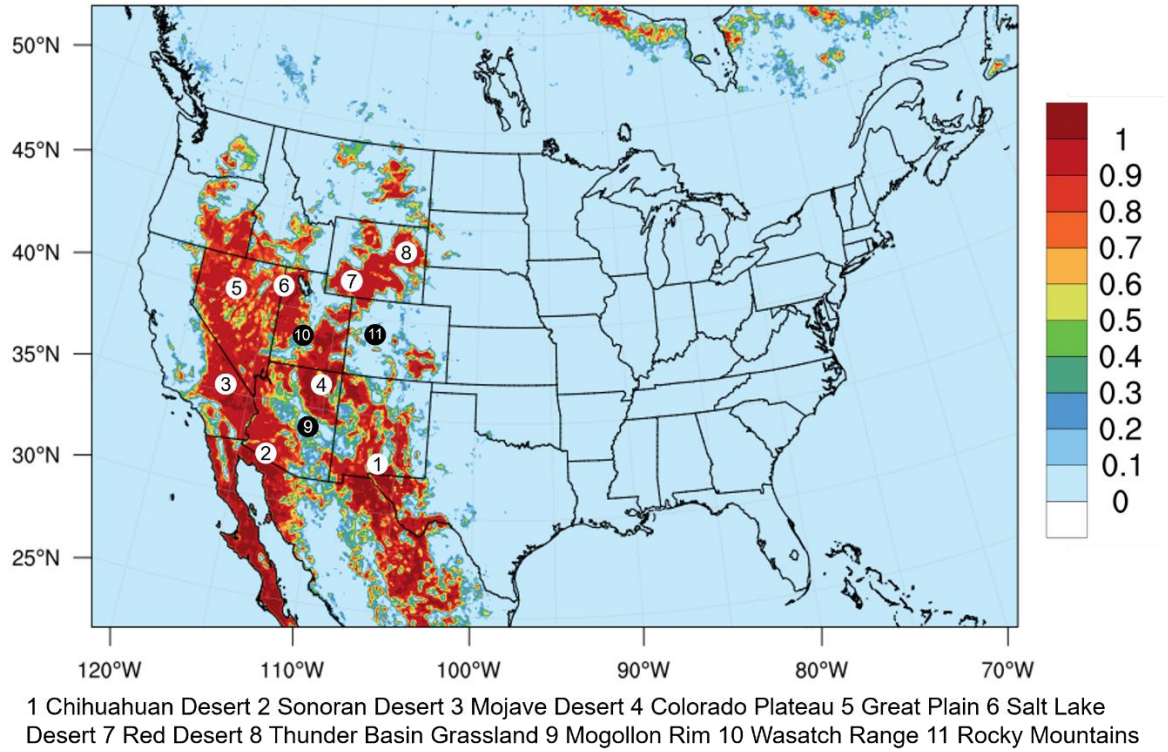

Figure 1. The total fractions of three types of erodible landuse (*USGS_shrubland*, *USGS_shrubgrass*, and *USGS_sprsbarren*) based on BELD3, along with annotations for geographic names used in this paper.

2.4. Evaluation Methodology

The windblown dust emissions in CMAQ are confined to erodible lands, so the evaluation of dust simulations was focused on the western states. Dust events are essential sources for minerals in the air. Therefore, we used observed “fine soil” (hereafter simply soil) concentrations as defined by the Interagency Monitoring of Protected Visual Environments (IMPROVE) sites (http://vista.cira.colostate.edu/Improve/) to evaluate the simulations. The IMPROVE network was designated to monitor the visibility in national parks and its sites concentrate in the western United States. The observatory data were available throughout 2016

every three days. The outputs from the CMAQ model were post-processed and the soil concentrations were calculated following the equation for soil adapted by the IMPROVE sites.

$$[Soil] = 2.2[Al] + 2.49[Si] + 1.63[Ca] + 2.42[Fe] + 1.94[Ti] \quad (8)$$

This equation considered the chemical composition of the oxides for predominant elements in soil (Malm, 1994).

The mean bias (MB), the normalized mean bias (NMB), the mean error (ME), the normalized mean error (NME), and the Pearson correlation coefficient between simulations and observations were used to access the simulated results.

3. Results and Discussion

3.1. Vegetation Coverage

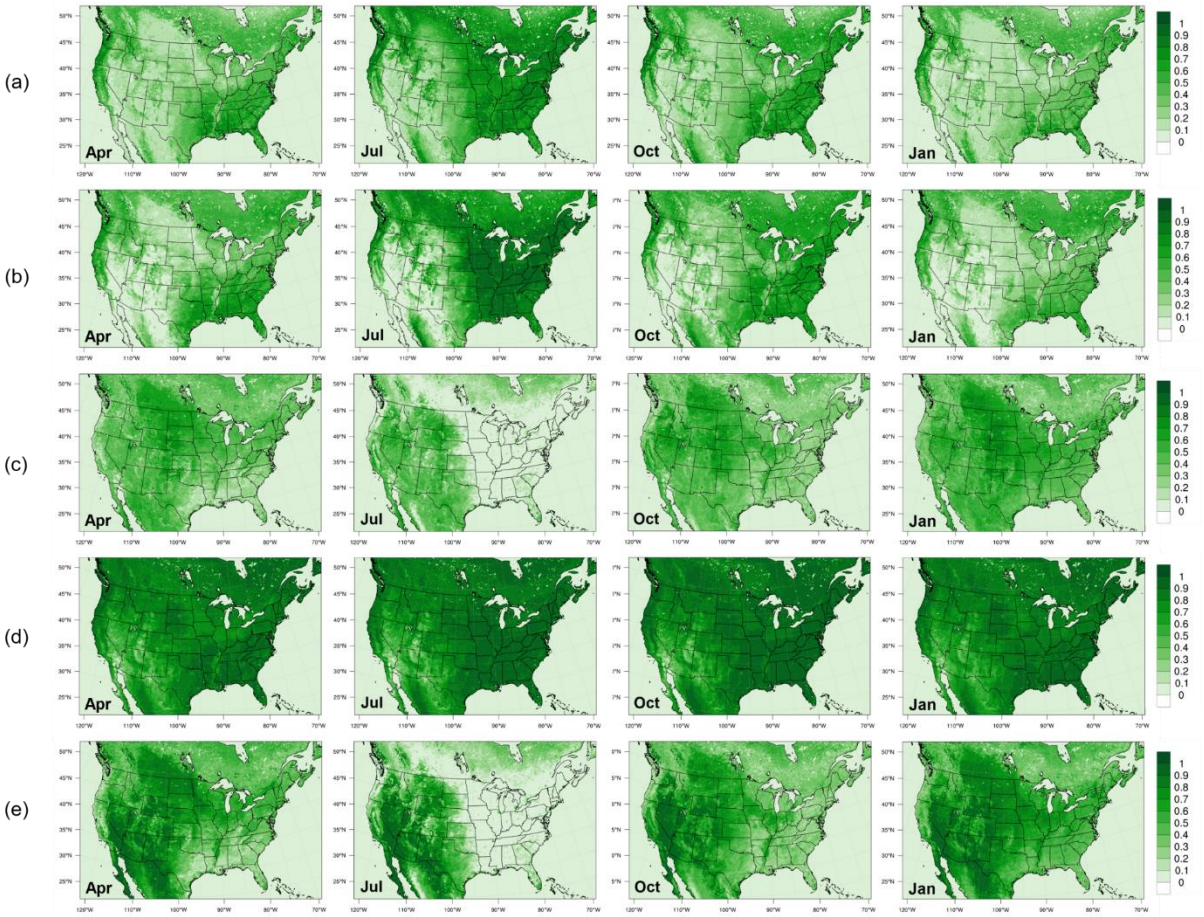

Figure 2. Spatial distributions of (a) the MODIS FPAR, (b) the PV fractions, (c) the NPV fractions, (d) the total vegetation fractions derived from MODIS surface reflectance using SMA, and (e) the ratio of NPV to total vegetation fractions at the 15th of the middle month in each season.

We present snapshots of the MODIS FPAR and the fractions of PV, NPV, and total vegetation obtained following procedures discussed in Sec. 2.1 in the middle of each season, as well as the ratio of NPV to total vegetation fractions in Figure 2. Clear contrasts between the eastern and the western parts of the region are seen in maps for green and brown vegetation (Figure 2(a)-(c)), which are most apparent in summer. The seasonal variation of both green and brown vegetation is higher in the east than in the west. Therefore, for the purpose of quantitative analysis, we averaged the vegetation fractions over the east and the west, separately. The separation was chosen to be along 97°W with consideration of both our vegetation maps and the shifted 100th meridian. The 100th meridian is a historical divide between the humid eastern and the arid western America, and it was found to shift eastwards due to climate change and human activities over past centuries (Seager, Feldman, et al., 2018; Seager, Lis, et al., 2018). The resulting averaged vegetation fractions from two datasets over the east and the west throughout 2016 are shown in Figure 3.

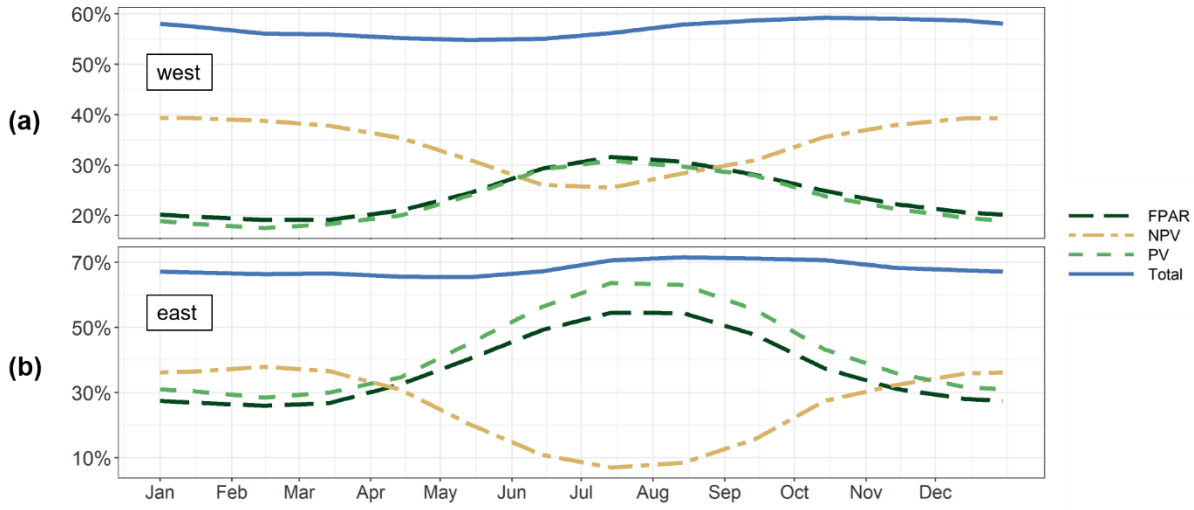

Figure 3. Averaged MODIS FPAR, PV, NPV, and total vegetation fractions over (a) the western and (b) the eastern study domain during 2016.

The vegetation fractions derived using the same SMA method were evaluated for Australia, and the RMSE for PV, NPV, and bare soil fractions were 0.13, 0.18, and 0.16, respectively (Guerschman et al., 2015). But these uncertainties are unknown for the vegetation data over the North America. To understand the reliability of the total vegetation maps, we compared the green vegetation coverage from two datasets. The MODIS FPAR (Figure 2(a)) and the PV fractions derived using the SMA technique (Figure 2(b)) agree well in spatial distribution across all seasons. Both of the coverages are relatively high in the Rocky Mountains, the Wasatch Range, and the Mogollon Rim in the western U.S., and they decrease northwestwards from the southeast coast in the eastern U.S. The averaged MODIS FPAR and SMA derived PV fractions differ by less than 9% in the east and 2% in the west throughout 2016. The comparable

values of PV fractions and MODIS FPAR demonstrate that the SMA method is generally good at resolving green vegetation over the study domain.

The NPV coverage in general has reversed spatial and temporal patterns relative to the green vegetation coverage. The percentage of NPV is relatively low in the forested regions in the west, and has a positive gradient in the Midwest. The average NPV fraction ranges between 26% and 40% over the western and between 7% and 36% over the eastern part of the CONUS (Figure 3). The average NPV fractions are at the minimum in late-June or mid-July, start to increase in August, and reach a maximum from December to February. These seasonal trends resemble the accumulation and decay of senescent plant materials. Note that, the maximum average coverage of NPV (40%) in 2016 exceeds that of PV (31%) in the west. This suggests that there may be other sources of NPV in the winter in addition to withered green vegetation from the same year, probably perennial dead biomass. This might also suggest some overestimations of NPV coverage using the SMA method. In the southwestern U.S., the averaged NPV fractions are high over most arid or semi-arid areas including the Chihuahuan Desert, the Colorado Plateau, the Great Basin, and the northern Great. The NPV coverage varies around 40%-50% across the year in these areas. In forested areas in the southwest where PV fractions are relatively high, the NPV coverage varies around 30% in 2016.

Maps for the ratios of NPV to total vegetation coverage or the relative ratios of NPV (Figure 2(e)) have similar spatial distribution as the NPV fractions, but with stronger contrasts. These maps highlight areas where NPV is the dominant component of vegetation. In the western U.S., the regions with high relative NPV ratio (nearly 100% in winter) greatly overlap with those with the erodible landuse. Most of these areas have high NPV coverage (> 40%in winter), except that the NPV fractions are relatively low (at around 30% in winter) in the Mojave Desert in the southmost corner of California. The relative ratios of NPV are constantly 100% in some southwestern desert lands all year round due to no detection of PV. In forested areas in the southwestern U.S., including the Mogollon Rim and the Rocky Mountains, the relative NPV ratio ranges between 20% and 70%.

The total vegetation coverage seems quite stable over the year (Figure 2(d)), as a result of the opposite spatial and seasonal trend of PV and NPV coverage. The average total vegetation fraction varies slightly around 56% in the west and around 68% in the east over the year. As expected, the coverage is relatively low in desert lands in the southwest. The annual average of total coverage is around 30% in the Great Basin, the Red Desert, the Sonoran Desert, the Colorado Plateau, and the Chihuahuan Desert, and it gradually increases towards the edges of these dry lands, reaching around 60% at the rims.

In the west, at places where NPV is abundant (both fractions and relative ratios), the PV is relatively sparse, and the total vegetation coverage is lower than other areas. These NPV-rich

regions highly overlap with regions with erodible landuse (see Figure 1). Therefore, NPV is expected to have an impact on dust emissions from these source regions.

3.2 Seasonal Analysis of Dust Emissions

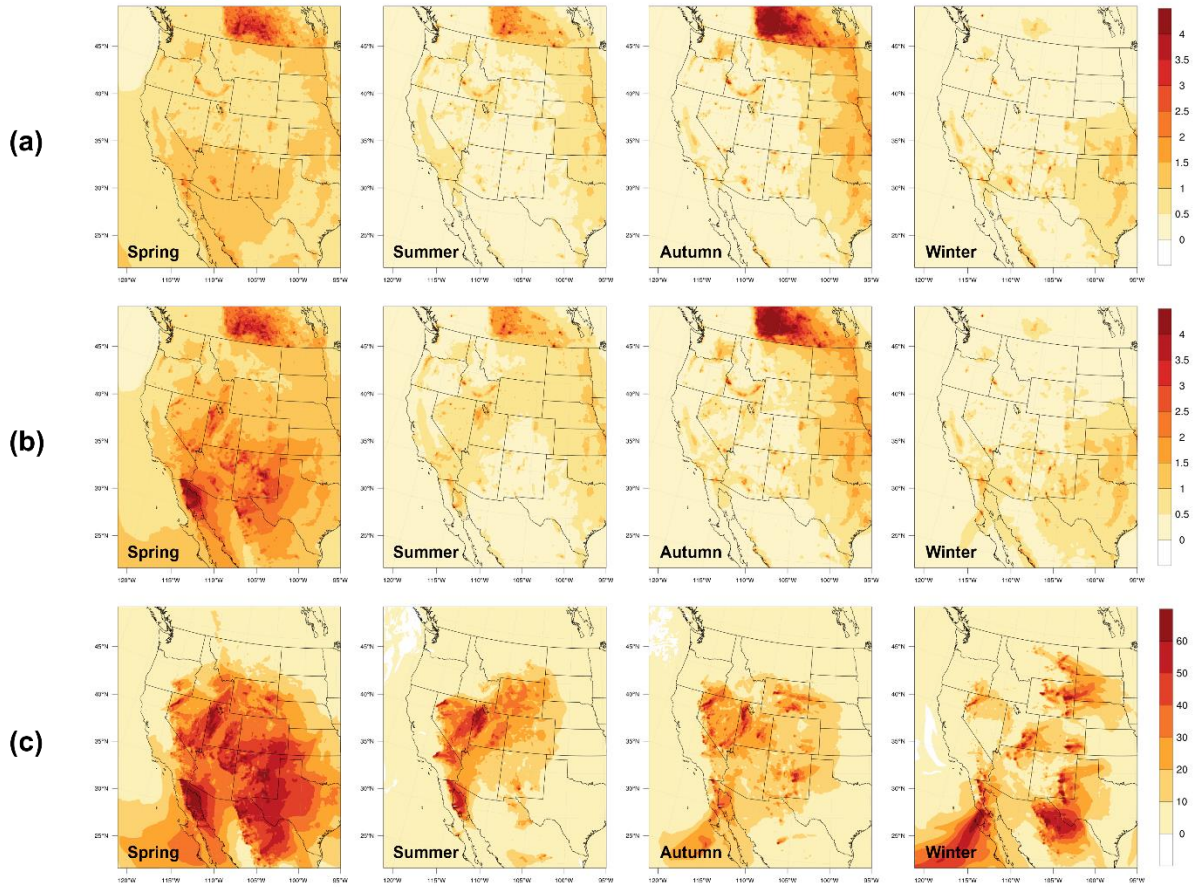

Figure 4. Seasonal averages of modeled soil concentrations (μg/m^3) over the western U.S. from (a) the TOTAL run and (b) the FPAR run. Row (c) presents the changes in soil concentrations (%) as percentage of soil concentrations from the FPAR run after replacing the MODIS FPAR data with the total vegetation data.

We presented the seasonal averages of simulated soil concentrations from the TOTAL run and the FPAR run in Figure 4(a) and (b), respectively. Comparisons among all seasons reveal that spring has the highest soil concentration for both cases. In spring, simulations from the TOTAL run show that the average soil concentrations are higher (above 1.5 μg/m^3) in the south, including most areas in Arizona and New Mexico, southern California, and northern Mexico, than other areas. As for the FPAR simulations, soil concentrations are consistently above 1.5 μg/m^3 over the southwestern U.S. during spring and the most pronounced soil concentrations (above 3 μg/m^3) are seen in several sub-regions with desert lands, including the Salt Lake Desert, the Colorado Plateau, the Sonoran Desert, and the Chihuahuan Desert. The

magnitude and spatial distribution of soil concentrations are comparable during summer and autumn for both cases, but more soils are emitted from the Great Basin in summer than in autumn in the FPAR run. The soil emissions in winter are similar to that in autumn, but less in northern states, probably due to snow cover. In general, simulations from both runs are able to capture the seasonal variation of dust emissions and highlight locations with high dust emissions.

Then, we analyzed the differences in simulated soil concentrations between the two runs to understand how NPV modulates windblown dust emissions. Figure 4(c) shows the changes in soil concentrations as percentage of the simulations from the FPAR run. Spring witnesses the most dramatic percentage of changes in soil concentrations in terms of affected areas. With the total vegetation data, the seasonal averaged soil concentrations reduce the most (above 50%) in dust source regions that generate the most soils in the FPAR run (Figure 4(b)) as mentioned above. The transport of emitted dust aerosols results in above 30% of changes in soil concentrations over most areas in the southwestern U.S. During summer, averaged soil concentrations reduce by over 50% in the Sonoran Desert and the Salt Lake Desert, and by over 20% also in the Mojave Desert, the Great Basin in Nevada, Wyoming, and western Colorado when using the total vegetation data. Changes in soil concentrations during autumn are less significant and over 50% of changes mainly occur over small areas in the Salt Lake Desert, northwestern Nevada, Wyoming, and eastern New Mexico. In winter, soil emissions are most suppressed by NPV in the same dust source regions as those for spring except for the Salt Lake Desert, and in eastern Montana additionally. The reductions in soil emissions by NPV, nevertheless, influence smaller areas downwind. Areas include the southern Nevada, western Utah, eastern Arizona, and western New Mexico experience less than 10% of change in soil concentrations, likely due to the relatively short-range transport of dust plumes.

Most areas in the southwestern U.S. experience above 10% of reductions in soil concentrations after replacing the MODIS FPAR data with the total vegetation data during all seasons but winter. Highest percentage (above 50%) of changes in soil concentrations are seen in dust source regions with high NPV fractions (> 40% in winter). Regions with large percentage of differences across multiple seasons highlight places where the dust emissions are most susceptible to NPV. These regions include the Sonoran Desert in Baja California, Mexico, the Chihuahuan Desert in New Mexico, the Great Basin in northwestern Nevada, and the Colorado Plateau in southeastern Utah, where the seasonal averaged soil concentrations are significantly suppressed by NPV throughout the year. Besides, the reductions in soil emissions induced by NPV are significant in the Salt Lake Desert throughout the year except in winter.

To shed light on the performances of the two model runs, we evaluated the simulations of soil concentrations from both runs with ground observations from the IMPROVE sites. The statistics of the models' performances over selected western states during each season are presented in Table 2. Selected states are Wyoming, Nevada, Utah, Colorado, Arizona, and New Mexico, which cover most of the active dust source regions in the U.S.

During spring, the normalized mean bias (NMB) of simulated soil concentrations from the TOTAL run (3.6%) is much smaller than that from the FPAR run (72.8%). The correlation coefficient between simulations and observations also increases from 0.44 to 0.52 when replacing MODIS FPAR with total vegetation. The similar results are seen in winter, when the NMB decreases by more than a half with total vegetation. In general, including NPV into the

model attenuates the overestimations of dust emissions during spring and winter. As discussed above, the effect of NPV on reducing dust overpredictions is more pronounced in spring than in winter, even though the NPV fractions are the highest in winter.

Both simulations, however, underpredict dust emissions during summer. The accuracy of simulations from the TOTAL run drops compared to those from the FPAR run, with the mean error increasing by around 0.1 $\mu g/m^3$. The underpredictions in summer are likely due to the inability of the model to capture small-scale convective storms, as discussed by several previous studies (Anisimov et al., 2018; Heinold et al., 2013; Pantillon et al., 2016). Foroutan and Pleim (2017) implemented lightning assimilation and sub-grid wind distribution in the CMAQ dust model to simulate convective storms, but these modifications were not included in this study, which probably explains the systematic negative biases. The effects of NPV on dust emissions after the convective storms are included need to be further analyzed. In autumn, the implementation of NPV slightly reduces the NME by 1.3%, but increases the magnitude of NMB by 9.8% and reduces the correlation coefficient by 0.06.

Table 2. Seasonal statistics for simulated soil concentrations from the FPAR run and the TOTAL run. Statistics are calculated for the western states of Wyoming, Nevada, Utah, Colorado, Arizona, and New Mexico. Observations are from the IMPROVE sites. Observation and simulation values, MB, and ME are in $\mu g/m^3$, and NMB and NME are in percent.

	Spring		Summer		Autumn		Winter	
	TOTAL	FPAR	TOTAL	FPAR	TOTAL	FPAR	TOTAL	FPAR
Observation	1.03		1.00		0.76		0.44	
Simulation	1.07	1.78	0.42	0.51	0.44	0.52	0.50	0.60
MB	0.04	0.75	-0.59	-0.50	-0.32	-0.24	0.06	0.17
NMB	3.6	72.8	-58.4	-49.5	-41.5	-31.7	14.5	37.9
ME	0.59	1.01	0.62	0.57	0.52	0.51	0.43	0.48
NME	57.4	97.9	61.8	56.4	67.9	66.6	98.4	110.0
Correlation	0.52	0.44	0.41	0.42	0.25	0.31	0.29	0.27
Number of observations	1175		1142		1155		1113	

We further investigated the spatial distribution of differences in model biases between the two runs. The seasonal averaged changes in biases after using total vegetation data is shown in Figure 5. During spring, the averaged biases in soil concentrations are lower for the TOTAL run at 93% of all IMPROVE sites. From the statistics in Table 2, we know the that these are reductions in overpredictions. The improvements are the greatest (up to 1.8 $\mu g/m^3$) in northern Arizona and New Mexico, southern Utah and Colorado, and west Wyoming. Slight reductions in overpredictions are also seen in southern California, Idaho and Montana. In contrast, simulations in southern Arizona are worsen because both cases underpredicted dust emissions here throughout the year. Reasons for the underpredictions might be the inability to model sub-grid dust events or the underestimation of amount of dust transported from outside the southeastern

border of the U.S. The changes in biases had the similar spatial distribution in winter but are less significant.

During summer, slight increases in biases (by 0.1-0.3 μg/m^3) from the TOTAL run are mostly seen in northwestern Arizona, Utah, northern Colorado, and northern Wyoming. Statistics from Table 2 reveal that inclusion of NPV intensifies the underpredictions of dust emissions in these areas. Averaged soil concentrations over autumn are comparable at most of the IMPROVE sites. The difference in biases fluctuates between -/+ 0.2 μg/m^3 with no apparent spatial characteristics.

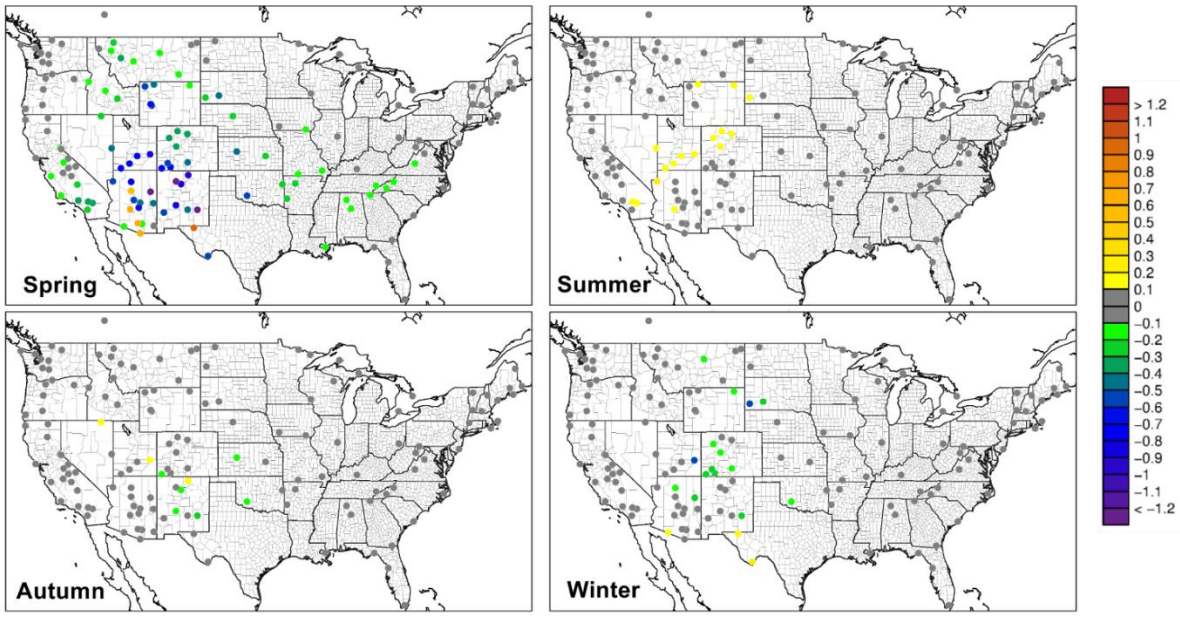

Figure 5. Seasonal averaged differences between the biases of soil concentrations (μg/m^3) from two runs. Observations are from the IMPROVE sites. Cold colors indicate that simulations from the TOTAL run have lower biases, thus the performance of TOTAL run is better. Warm colors indicate that the FPAR run performs better.

3.3. Mechanisms of Dust Emission Suppression

Vegetation modulates windblown dust emissions through multiple pathways. An in-depth comparison between the FPAR run and the TOTAL run simulations allows us to understand different mechanisms by which NPV impacts windblown dust emissions.

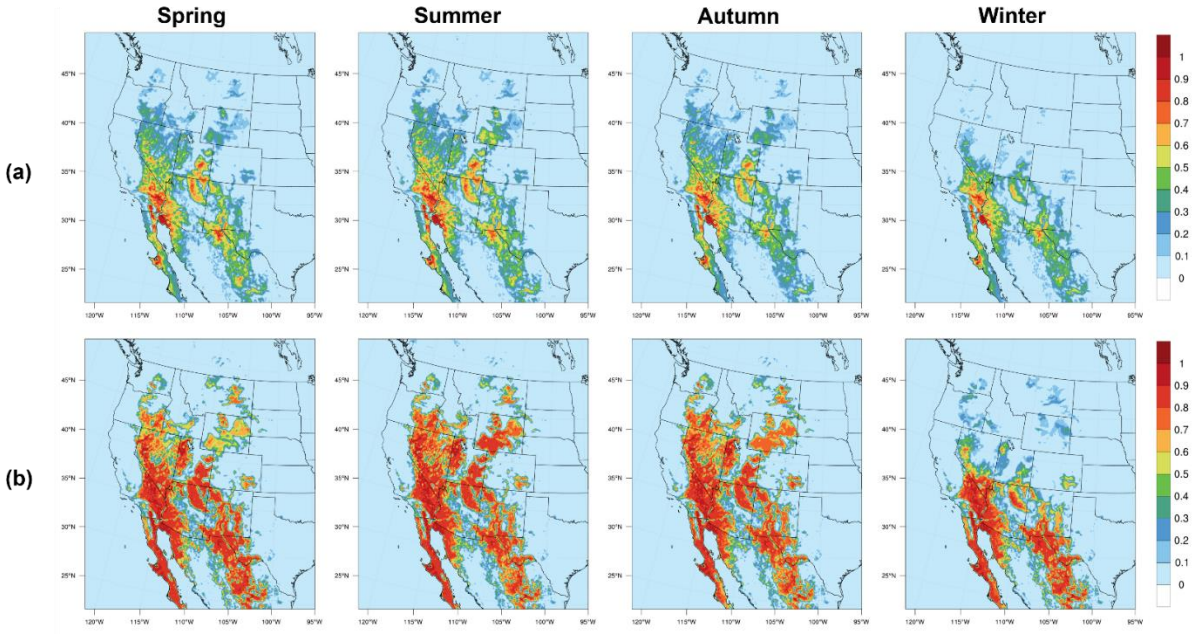

Figure 6. Seasonal averaged fractions of vegetation-free erodible lands from (a) the TOTAL run and (b) the FPAR run.

First, the vegetation coverage directly controls the fraction of land susceptible to wind erosion. In the model, the total vertical flux of dust is calculated as the weighted sum of fluxes from three erodible landuse (see Figure 1) multiplied by the fraction of land that is not covered with vegetation in each grid cell. The mechanism considered here is that vegetation covering the bare soil prevents the saltating particles from impacting the surface and smaller dust particles from being ejected to the atmosphere.

Figure 6 presents the fractions of vegetation-free land available for dust emissions from the two cases. The decrease in the fractions of land susceptible to dust emission is significant in all seasons after the PV is replaced with the total vegetation in the model. The reduction is the largest in autumn, followed by summer, and is comparable in spring and winter. Places with the most changes are the Salt Lake Desert, the northern Great Plain located in Nevada, Oregon, and Idaho, the northeastern Wyoming, and Montana, where the vegetation-free erodible lands decrease by over 50% in autumn. In most grid cells containing dust sources, the fractions of vegetation-free erodible lands decrease by over 0.2 in all seasons. Because the total emission of dust from each grid cell is proportional to the fractions of vegetation-free erodible land, these significant reductions suggest that one strong mechanism for NPV to reduce dust emission is to

prevent dust particles from leaving the surface. Nevertheless, potential underestimation of dust emissions when using total vegetation may occur due to two reasons. First, the actual fractions of land available to dust emission may be underestimated because the vegetation on non-erodible lands should not affect the exposed areas with erodible landuse. Higher resolution of landuse and vegetation inputs should help to address this issue. Second, this mechanism of dust suppression is only true for vegetation that is closer to the ground. Some NPV, such as standing dead trees, are detected by the satellite but cannot prevent soil erosion through this pathway.

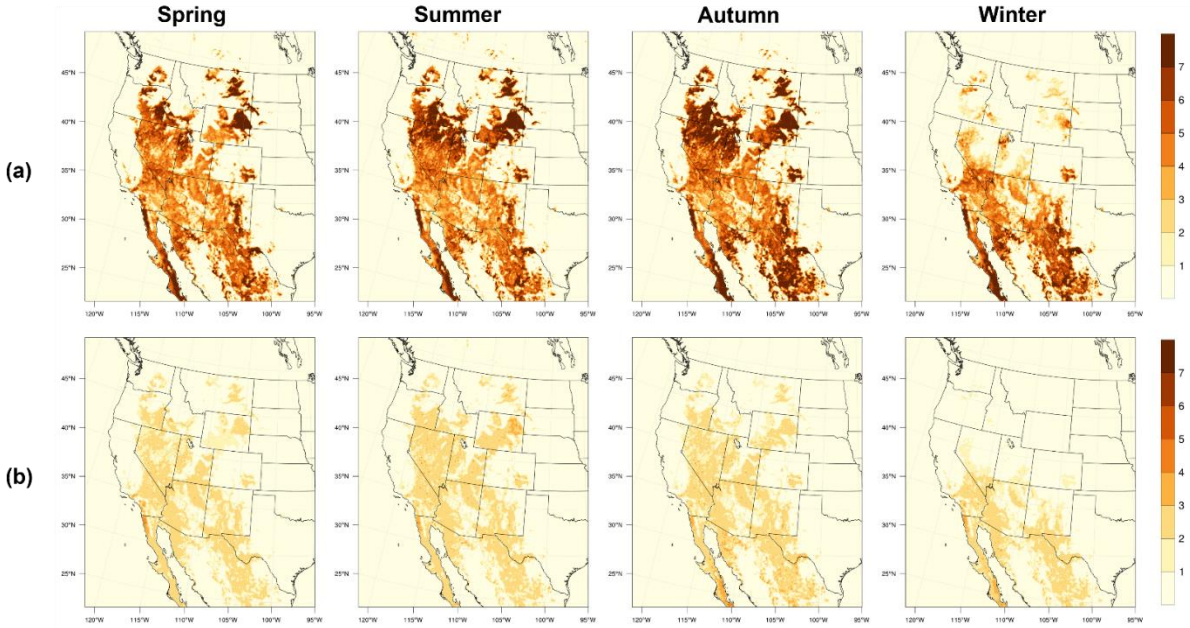

Figure 7. Seasonal averages of the roughness correction factors for the threshold velocity from (a) the TOTAL run and (b) the FPAR run. Values were calculated as the averages of roughness correction factors on three erodible landuse types weighted by the fractions of each landuse.

Second, the initiation of dust generation is jointly controlled by the friction velocity and its threshold value (see Eqn. 1). Emissions of windblown dust can only occur and sustain when the friction velocity exceeds the threshold velocity. Our results show that several peaks in the simulated particle concentrations in the FPAR case are absent in the TOTAL case, especially during spring. This observation suggests that NPV may prevent a number of the dust events from happening by either increasing the threshold velocity or decreasing the friction velocity, or both. Given this, we investigated the differences in modeled threshold velocity between the two simulations. Vegetation can increase the threshold velocity by extracting the wind stress exerted on the ground surface through drag partitioning process (Foroutan et al., 2017). In our model, the threshold velocity was calculated as the ideal threshold velocity modified by correction factors for soil moisture and surface roughness (see Eqn. 2). The inclusion of NPV would not change the ideal threshold velocity or soil moisture (vegetation can affect soil moisture by intercepting rainfall and uptake soil water (Teuling, 2005), but these interactions were not implemented in our

model), so the change in the correction factor for surface roughness can reflect the change in magnitude of threshold velocity.

We illustrate the seasonal averages of the correction factor for roughness calculated as the average of correction factors for three erodible landuse types weighted by the fractions of each type in Figure 7. In practice, the model actually uses the roughness correction factor separately over each landuse types, and the values shown here were not used directly in the model. However, they serve as a good representation of the magnitude of overall roughness correction factor. Seasonal averaged roughness factor is below 3 in most places across the year for the FPAR run, but significantly increases in most areas for the TOTAL run. Largest changes in roughness factor are seen in the northern Great Basin, Wyoming, Montana, western Colorado, and in the Chihuahuan Desert and the Sonoran Desert, where the averaged changes are over 4 in autumn. These NPV induced increases in roughness factor would raise the threshold velocity by over 50% in most areas and over 200% in places such as northeastern Wyoming, and hence lessen the potential for dust emissions in these regions.

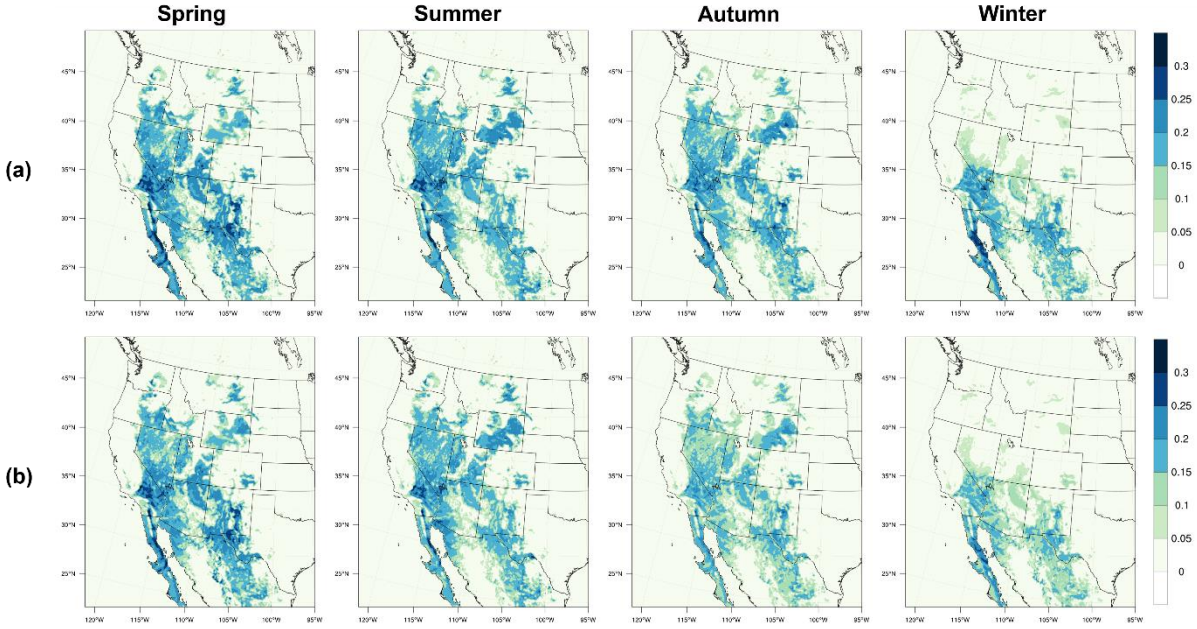

Figure 8. Seasonal averages of the friction velocity from (a) the TOTAL run and (b) the FPAR run. Values were calculated as the averages of the friction velocities on three edible landuse types weighted by the fractions of each landuse.

Third, vegetation can impact the friction velocity itself. Friction velocity is not only associated with the initiation of dust events, but also essential in determining the dust flux. The horizontal flux of dust is proportional to the third power of the friction velocity (Eq. (1)) and is thus very sensitive to its value. Vegetation elements that protrude the ground can alter the wind profile and thus change the friction velocity exerted on the surface. The effect of vegetation on

wind profile was accounted for using roughness length, which has a non-linear relation with roughness density or fractional cover of vegetation (Eqn. (5, 6)).

We present the seasonal averages of the weighted mean friction velocity in Figure 8, calculated using the same method as for the roughness factor. Non-linear effects of NPV on the friction velocities are observed. During spring and summer, the friction velocity increases by less than 0.02 m/s (below 10%) in most places, by 20-30% in the Salt Lake Desert, and decreases in northeastern Wyoming and southeastern Colorado with the inclusion of NPV. In autumn and winter, the increases in friction velocity due to NPV are more significant, reaching 0.03-0.05 m/s (10-20%) on most erodible lands. Considering that the friction velocity increases in most of the erodible lands with inclusion of NPV, which would facilitate the initiation of saltation, we can conclude that the observed preventions of dust events are mainly attributed to the increases in threshold velocity. However, a sensitivity analysis (Darmenova et al., 2009) showed that the percentage of increase in friction velocity could lead to up to two orders of magnitude increase in the dust flux when the wind velocity is low (less than 0.05 m/s), which is our case. So the increases in friction velocity caused by NPV could potentially amplify the dust flux by considerable amounts.

4. Conclusions

This paper analyzed the effects of NPV on the amount of windblown dust emissions, and the underlying mechanisms on a regional scale. We implemented satellite-based total vegetation data, which include both photosynthetic (PV) and non-photosynthetic vegetation (NPV), in the dust module in CMAQ version 5.3 and conducted simulations for a domain covering the conterminous United States for the entire year 2016. The fractional coverage of total vegetation was derived from the MODIS surface reflectance data using a spectral mixture analysis (SMA) method. A control run was conducted using the Moderate Resolution Imaging Spectroradiometer (MODIS) Fraction of Absorbed Photosynthetically Active Radiation (FPAR) data which merely presented PV fractions.

The PV fractions derived from the SMA approach and the MODIS FPAR have similar spatial distributions across all seasons, and the difference between their averages over the western U.S. are less than 2% for the entire year. The average NPV fraction over the western part of the study domain is maximum from December to February and shows a minimum from June to August, ranging between 26% and 40%. Higher peak in the NPV coverage compared to that of the PV coverage indicates that there are sources for NPV other than senescent plant materials from the same year, probably perennial dry vegetation. The NPV coverage was around 40%-50% over most of the arid and semi-arid areas in the southwestern U.S. throughout the year. The areas with high NPV-to-total-vegetation ratios highly overlap with the areas covered by erodible landuse, suggesting that consideration of NPV was important for dust emissions from the source regions.

Simulations of soil concentrations from both the TOTAL run and the FPAR run present the seasonal variation of dust emissions and highlight locations with high dust emissions. We analyzed the averaged percentage of differences in simulated soil concentrations between the two simulations for all seasons. Simulated soil concentrations decrease by above 10% due to NPV in most areas in southwestern U.S. from spring to autumn, and these affected areas are more

confined in winter. NPV induced reductions in soil concentrations are most significant in spring. Regions with above 50% of reductions in soil concentrations over the entire year exclusively have high NPV fractions (< 40% in winter), including parts of the Sonoran Desert, the Chihuahuan Desert in New Mexico, the Great Basin in northwestern Nevada, and the Colorado Plateau in southeastern Utah. Evaluation of soil concentrations against the IMPROVE observations reveals that inclusion of NPV in the dust model attenuates the overpredictions at 93% of the sites during spring, except for those near southern Arizona. In summer, however, the underpredictions in soil concentrations are accentuated, especially in Utah, Colorado, and Wyoming, which potentially could be improved by implementing convective storms simulations in the dust model.

Analyses of several parameters in the dust model to the inclusion of NPV provide insights into the mechanisms by which NPV modulates dust emissions. The fraction of land susceptible to wind erosion is reduces by 20% in most grid cells due to NPV, indicating that NPV effectively prevents dust particles from being ejected from the ground by covering the land surface. The prevention of several dust events resulted from NPV are associated with the increases in threshold velocity and, in limited places, the decreases in friction velocity. On most erodible lands, however, the friction velocity increases by above 10% in autumn and winter, which could potentially amplify the dust flux by a few times.

This paper points out that dust emissions from a large portion of erodible lands are modulated by the NPV. Therefore, replacing the green vegetation data currently used in many dust models with the total vegetation data derived from satellite-based surface reflectance is a promising approach to improve the simulations of dust emissions, and thus advance the knowledge of the health impact, climate effects, and global cycling of nutrients associated with windblown dust aerosols. Meanwhile, more evaluation of the calculated NPV and total vegetation fractions is needed to better understand the uncertainties associated with the vegetation input, which will facilitate the implementation of NPV into atmospheric dust models.

Acknowledgments

This work was supported by the United States Environmental Protection Agency (US EPA) under the grant number 68HERC20Q0015. We thank J. P. Guerschman for assistance with the vegetation data. The fractional coverage data of total vegetation is available at https://eo-data.csiro.au/remotesensing/v310/global_5km. Data used in this analysis are available via the Virginia Tech research repository (https://doi.org/xxxxxxxxxxxxx). CMAQ source code is freely available via https://github.com/usepa/cmaq.git. Archived CMAQ versions are available from the same repository. Model input data are available from the Community Modeling and Analysis System (CMAS) Data Warehouse (https://doi.org/10.15139/S3/MHNUNE). The authors declare that there is no conflict of interest related to this work.

References

Al-Hemoud, A., Al-Dousari, A., Misak, R., Al-Sudairawi, M., Naseeb, A., Al-Dashti, H., & Al-Dousari, N. (2019). Economic Impact and Risk Assessment of Sand and Dust Storms (SDS) on the Oil and Gas Industry in Kuwait. *Sustainability, 11*(1). doi:10.3390/su11010200

Anisimov, A., Axisa, D., Kucera, P. A., Mostamandi, S., & Stenchikov, G. (2018). Observations and Cloud-Resolving Modeling of Haboob Dust Storms Over the Arabian Peninsula. *Journal of Geophysical Research: Atmospheres, 123*(21), 12147-12179. doi:10.1029/2018JD028486

Appel, K. W., Bash, J. O., Fahey, K. M., Foley, K. M., Gilliam, R. C., Hogrefe, C., . . . Wong, D. C. (2020). The Community Multiscale Air Quality (CMAQ) Model Versions 5.3 and 5.3.1: System Updates and Evaluation. *Geosci. Model Dev. Discuss., 2020*, 1-41. doi:10.5194/gmd-2020-345

Asner, G. P., & Heidebrecht, K. B. (2002). Spectral unmixing of vegetation, soil and dry carbon cover in arid regions: Comparing multispectral and hyperspectral observations. *International Journal of Remote Sensing, 23*(19), 3939-3958. doi:10.1080/01431160110115960

Baddock, M. C., Strong, C. L., Leys, J. F., Heidenreich, S. K., Tews, E. K., & McTainsh, G. H. (2014). A visibility and total suspended dust relationship. *Atmospheric Environment, 89*, 329-336. doi:https://doi.org/10.1016/j.atmosenv.2014.02.038

Cao, X., Chen, J., Matsushita, B., & Imura, H. (2010). Developing a MODIS-based index to discriminate dead fuel from photosynthetic vegetation and soil background in the Asian steppe area. *International Journal of Remote Sensing, 31*(6), 1589-1604. doi:10.1080/01431160903475274

Csavina, J., Field, J., Taylor, M. P., Gao, S., Landazuri, A., Betterton, E. A., & Saez, A. E. (2012). A review on the importance of metals and metalloids in atmospheric dust and aerosol from mining operations. *Sci Total Environ, 433*, 58-73. doi:10.1016/j.scitotenv.2012.06.013

Darmenova, K., Sokolik, I. N., Shao, Y., Marticorena, B., & Bergametti, G. (2009). Development of a physically based dust emission module within the Weather Research and Forecasting (WRF) model: Assessment of dust emission parameterizations and input parameters for source regions in Central and East Asia. *Journal of Geophysical Research, 114*(D14). doi:10.1029/2008jd011236

Duncan Fairlie, T., Jacob, D. J., & Park, R. J. (2007). The impact of transpacific transport of mineral dust in the United States. *Atmospheric Environment, 41*(6), 1251-1266. doi:10.1016/j.atmosenv.2006.09.048

F. FeÂcan, B. M. a. G. B. (1999). Parametrization of the increase of the aeolian erosion threshold wind friction velocity due to soil moisture for arid and semi-arid areas. *Annales Geophysicae*.

Foroutan, H., & Pleim, J. E. (2017). Improving the simulation of convective dust storms in regional-to-global models. *J Adv Model Earth Syst, 9*(5), 2046-2060. doi:10.1002/2017MS000953

617 Foroutan, H., Young, J., Napelenok, S., Ran, L., Appel, K. W., Gilliam, R. C., & Pleim, J. E. (2017).
618 Development and evaluation of a physics-based windblown dust emission scheme
619 implemented in the CMAQ modeling system. *J Adv Model Earth Syst, 9*(1), 585-608.
620 doi:10.1002/2016MS000823

621 Guerschman, Hill, M. J., Renzullo, L. J., Barrett, D. J., Marks, A. S., & Botha, E. J. (2009).
622 Estimating fractional cover of photosynthetic vegetation, non-photosynthetic vegetation
623 and bare soil in the Australian tropical savanna region upscaling the EO-1 Hyperion and
624 MODIS sensors. *Remote Sensing of Environment, 113*(5), 928-945.
625 doi:10.1016/j.rse.2009.01.006

626 Guerschman, Scarth, P. F., McVicar, T. R., Renzullo, L. J., Malthus, T. J., Stewart, J. B., . . .
627 Trevithick, R. (2015). Assessing the effects of site heterogeneity and soil properties when
628 unmixing photosynthetic vegetation, non-photosynthetic vegetation and bare soil fractions
629 from Landsat and MODIS data. *Remote Sensing of Environment, 161*, 12-26.
630 doi:10.1016/j.rse.2015.01.021

631 Hagen, L. J. (1996). Crop Residue Effects On Aerodynamic Processes and Wind Erosion.
632 *Theoretical and Applied Climatology*.

633 Heinold, B., Knippertz, P., Marsham, J. H., Fiedler, S., Dixon, N. S., Schepanski, K., . . . Tegen, I.
634 (2013). The role of deep convection and nocturnal low-level jets for dust emission in
635 summertime West Africa: Estimates from convection-permitting simulations. *J Geophys*
636 *Res Atmos, 118*(10), 4385-4400. doi:10.1002/jgrd.50402

637 Ji, C., Li, X., Wei, H., & Li, S. (2020). Comparison of Different Multispectral Sensors for
638 Photosynthetic and Non-Photosynthetic Vegetation-Fraction Retrieval. *Remote Sensing,*
639 *12*(1). doi:10.3390/rs12010115

640 Kang, J.-Y., Tanaka, T. Y., & Mikami, M. (2014). Effect of dead leaves on early spring dust
641 emission in East Asia. *Atmospheric Environment, 86*, 35-46.
642 doi:10.1016/j.atmosenv.2013.12.007

643 Kellogg, C. A., & Griffin, D. W. (2006). Aerobiology and the global transport of desert dust. *Trends*
644 *Ecol Evol, 21*(11), 638-644. doi:10.1016/j.tree.2006.07.004

645 Klose, M., Jorba, O., Gonçalves Ageitos, M., Escribano, J., Dawson, M. L., Obiso, V., . . . Pérez
646 García-Pando, C. (2021). Mineral dust cycle in the Multiscale Online Nonhydrostatic
647 AtmospheRe CHemistry model (MONARCH) Version 2.0. *Geosci. Model Dev. Discuss.*
648 doi:10.5194/gmd-2021-32

649 Knippertz, P. (2017). Mineral Dust Generation across Northern Africa and Its Impacts. In *Oxford*
650 *Research Encyclopedia of Climate Science*.

651 Kurosaki, Y., Shinoda, M., Mikami, M., & Nandintsetseg, B. (2011). Effects of Soil and Land
652 Surface Conditions in Summer on Dust Outbreaks in the Following Spring in a Mongolian

Grassland. *SOLA, 7*, 69-72. doi:10.2151/sola.2011-018

LeGrand, S. L., Polashenski, C., Letcher, T. W., Creighton, G. A., Peckham, S. E., & Cetola, J. D. (2019). The AFWA dust emission scheme for the GOCART aerosol model in WRF-Chem v3.8.1. *Geoscientific Model Development, 12*(1), 131-166. doi:10.5194/gmd-12-131-2019

Li, X., Zheng, G., Wang, J., Ji, C., Sun, B., & Gao, Z. (2016). Comparison of Methods for Estimating Fractional Cover of Photosynthetic and Non-Photosynthetic Vegetation in the Otindag Sandy Land Using GF-1 Wide-Field View Data. *Remote Sensing, 8*(10). doi:10.3390/rs8100800

Li, Z., & Guo, X. (2015). Remote sensing of terrestrial non-photosynthetic vegetation using hyperspectral, multispectral, SAR, and LiDAR data. *Progress in Physical Geography: Earth and Environment, 40*(2), 276-304. doi:10.1177/0309133315582005

Lin, X., Niu, J., Yu, X., Berndtsson, R., Wu, S., & Xie, S. (2021). Maize residue effects on PM2.5, PM10, and dust emission from agricultural land. *Soil and Tillage Research, 205*. doi:10.1016/j.still.2020.104738

Lu, H., & Shao, Y. (1999). A new model for dust emission by saltation bombardment. *Journal of Geophysical Research: Atmospheres, 104*(D14), 16827-16842. doi:10.1029/1999jd900169

Malm, W. C. (1994). Spatial and seasonal trends in particle concentration and optical extinction in the United States. *Journal of Geophysical Research, VOL. 99, NO. D1, PAGES 1347-137*.

Marsett, R. C., Qi, J., Heilman, P., Biedenbender, S. H., Carolyn Watson, M., Amer, S., . . . Marsett, R. (2006). Remote Sensing for Grassland Management in the Arid Southwest. *Rangeland Ecology & Management, 59*(5), 530-540. doi:10.2111/05-201r.1

Mougin, E., Lo Seen, D., Ramba, S., Gaston, A., & Hiernaux, P. (1995). A Regional Sahelian Grassland Model To Be Coupled with Multispectral Satellite Data. I: Model Description and Validation.

Nakao, M., Ishihara, Y., Kim, C. H., & Hyun, I. G. (2018). The Impact of Air Pollution, Including Asian Sand Dust, on Respiratory Symptoms and Health-related Quality of Life in Outpatients With Chronic Respiratory Disease in Korea: A Panel Study. *J Prev Med Public Health, 51*(3), 130-139. doi:10.3961/jpmph.18.021

Nandintsetseg, B., & Shinoda, M. (2015). Land surface memory effects on dust emission in a Mongolian temperate grassland. *Journal of Geophysical Research-Biogeosciences, 120*(3), 414-427. doi:10.1002/2014jg002708

Okin, G. S., Clarke, K. D., & Lewis, M. M. (2013). Comparison of methods for estimation of absolute vegetation and soil fractional cover using MODIS normalized BRDF-adjusted reflectance data. *Remote Sensing of Environment, 130*, 266-279. doi:10.1016/j.rse.2012.11.021

688 Pantillon, F., Knippertz, P., Marsham, J. H., Panitz, H.-J., & Bischoff-Gauss, I. (2016). Modeling
689 haboob dust storms in large-scale weather and climate models. *Journal of Geophysical*
690 *Research: Atmospheres, 121*(5), 2090-2109. doi:10.1002/2015jd024349

691 Pierre, C., Kergoat, L., Bergametti, G., Mougin, É., Baron, C., Abdourhamane Toure, A., . . . Delon,
692 C. (2015). Modeling vegetation and wind erosion from a millet field and from a rangeland:
693 Two Sahelian case studies. *Aeolian Research, 19*, 97-111.
694 doi:10.1016/j.aeolia.2015.09.009

695 Qi, J., & Wallace, O. (2002). Biophysical Attributes Estimation from Satellite Images in Arid
696 Regions.

697 R. L. Miller, I. T. (1998). Climate Response to Soil Dust Aerosols. *Journal of Climate*.

698 Ran, L., Pleim, J., Gilliam, R., Binkowski, F. S., Hogrefe, C., & Band, L. (2016). Improved
699 meteorology from an updated WRF/CMAQ modeling system with MODIS vegetation and
700 albedo. *Journal of Geophysical Research: Atmospheres, 121*(5), 2393-2415.
701 doi:10.1002/2015jd024406

702 Raupach, M. R., Gillette, D. A., & Leys, J. F. (1993). The effect of roughness elements on wind
703 erosion threshold. *Journal of Geophysical Research: Atmospheres, 98*(D2), 3023-3029.
704 doi:https://doi.org/10.1029/92JD01922

705 Scarth, P. F., Röder, A., & Schmidt, M. (2011). *Tracking Grazing Pressure and Climate Interaction*
706 *- The Role of LANDSAT Fractional Cover in Time Series Analysis.* Paper presented at the
707 Proceedings of the 15th Australasian Remote Sensing and Photogrammetry Conference,
708 Australia: Alice Springs.

709 Seager, R., Feldman, J., Lis, N., Ting, M., Williams, A. P., Nakamura, J., . . . Henderson, N. (2018).
710 Whither the 100th Meridian? The Once and Future Physical and Human Geography of
711 America's Arid–Humid Divide. Part II: The Meridian Moves East. *Earth Interactions,*
712 *22*(5), 1-24. doi:10.1175/ei-d-17-0012.1

713 Seager, R., Lis, N., Feldman, J., Ting, M., Williams, A. P., Nakamura, J., . . . Henderson, N. (2018).
714 Whither the 100th Meridian? The Once and Future Physical and Human Geography of
715 America's Arid–Humid Divide. Part I: The Story So Far. *Earth Interactions, 22*(5), 1-22.
716 doi:10.1175/ei-d-17-0011.1

717 Shao, Y. P., Raupach, M. R., & Leys, J. F. (1996). A model for predicting aeolian sand drift and
718 dust entrainment on scales from paddock to region. *Soil Research, 34*(3), 309-342.
719 Retrieved from https://doi.org/10.1071/SR9960309

720 Shinoda, M., Gillies, J. A., Mikami, M., & Shao, Y. (2011). Temperate grasslands as a dust source:
721 Knowledge, uncertainties, and challenges. *Aeolian Research, 3*(3), 271-293.
722 doi:10.1016/j.aeolia.2011.07.001

723 Tegen, I., Harrison, S. P., Kohfeld, K., Prentice, I. C., Coe, M., & Heimann, M. (2002). Impact of
724 vegetation and preferential source areas on global dust aerosol: Results from a model study.
725 *Journal of Geophysical Research: Atmospheres, 107*(D21), AAC 14-11-AAC 14-27.
726 doi:10.1029/2001jd000963

727 Teuling, A. J. (2005). Improved understanding of soil moisture variability dynamics. *Geophysical*
728 *Research Letters, 32*(5). doi:10.1029/2004gl021935

729 Xi, X., & Sokolik, I. N. (2015). Seasonal dynamics of threshold friction velocity and dust emission
730 in Central Asia. *Journal of Geophysical Research: Atmospheres, 120*(4), 1536-1564.
731 doi:10.1002/2014jd022471

732 Zhang, K., O'Donnell, D., Kazil, J., Stier, P., Kinne, S., Lohmann, U., . . . Feichter, J. (2012). The
733 global aerosol-climate model ECHAM-HAM, version 2: sensitivity to improvements in
734 process representations. *Atmospheric Chemistry and Physics, 12*(19), 8911-8949.
735 doi:10.5194/acp-12-8911-2012